Article

Demonstration of a trapped-ion atomic clock in space

https://doi.org/10.1038/s41586-021-03571-7

Received: 4 December 2020

Accepted: 21 April 2021

Published online: 30 June 2021

Check for updates

E. A. Burt[1,2]✉, J. D. Prestage[1,2], R. L. Tjoelker[1,2], D. G. Enzer[1], D. Kuang[1], D. W. Murphy[1], D. E. Robison[1], J. M. Seubert[1], R. T. Wang[1] & T. A. Ely[1]

Atomic clocks, which lock the frequency of an oscillator to the extremely stable quantized energy levels of atoms, are essential for navigation applications such as deep space exploration[1] and global navigation satellite systems[2], and are useful tools with which to address questions in fundamental physics[3–6]. Such satellite systems use precise measurement of signal propagation times determined by atomic clocks, together with propagation speed, to calculate position. Although space atomic clocks with low instability are an enabling technology for global navigation, they have not yet been applied to deep space navigation and have seen only limited application to space-based fundamental physics, owing to performance constraints imposed by the rigours of space operation[7]. Methods of electromagnetically trapping and cooling ions have revolutionized atomic clock performance[8–13]. Terrestrial trapped-ion clocks operating in the optical domain have achieved orders-of-magnitude improvements in performance over their predecessors and have become a key component in national metrology laboratory research programmes[13], but transporting this new technology into space has remained challenging. Here we show the results from a trapped-ion atomic clock operating in space. On the ground, NASA's Deep Space Atomic Clock demonstrated a short-term fractional frequency stability of $1.5 \times 10^{-13}/\tau^{1/2}$ (where τ is the averaging time)[14]. Launched in 2019, the clock has operated for more than 12 months in space and demonstrated there a long-term stability of 3×10^{-15} at 23 days (no drift removal), and an estimated drift of $3.0(0.7) \times 10^{-16}$ per day. Each of these exceeds current space clock performance by up to an order of magnitude[15–17]. The Deep Space Atomic Clock is particularly amenable to the space environment because of its low sensitivity to variations in radiation, temperature and magnetic fields. This level of space clock performance will enable one-way navigation in which signal delay times are measured in situ, making near-real-time navigation of deep space probes possible[18].

All space clocks in use today employ atomic beams or gas cells to confine atoms[15–17]. These clocks have short-term stabilities ranging from $1 \times 10^{-12}/\tau^{1/2}$ to $10 \times 10^{-12}/\tau^{1/2}$, whereas long-term (greater than a day) stability, usually characterized by drift, is between 1×10^{-15} and 10×10^{-15} per day. Long-term clock autonomy, highly desirable for deep space and global navigation satellite system (GNSS) applications[19], is limited by drift, which in cell clocks is usually caused by wall collisions. Trapped-ion clocks[20] solve this by electromagnetically confining atoms, thereby eliminating wall collisions. Recently, a different type of beam clock was demonstrated in space with an inferred short-term stability of $3 \times 10^{-13}/\tau^{1/2}$ (ref. [21]), but no long-term stability was reported.

Because of the advantages to clock performance provided by atom trapping, many primary atomic clocks used in national metrology laboratories use some form of trapping[12,13]. Motivated by the low instability of trapped-ion clocks and by their potentially very small size, NASA's Jet Propulsion Laboratory (JPL) embarked on a series of mercury ion clock development projects aimed at ultimately producing a space-qualified version. Demonstrations in the laboratory achieved a stability of $2 \times 10^{-14}/\tau^{1/2}$ (ref. [10]) and drifts as low as 2.7×10^{-17} per day (no drift removal)[11]. The approach followed at JPL did not use lasers, cryogenics or microwave cavities, enabling the technology to be robust and relatively small, and to consume less than 50 W of power[10,22–24].

Following this success, in 2011 NASA's Space Technology Mission Directorate initiated the Deep Space Atomic Clock (DSAC) mission to demonstrate a trapped-ion atomic clock in space with the goal of $2 \times 10^{-13}/\tau^{1/2}$ short-term stability and a non-drift-removed 3×10^{-15} stability at one day. This technology demonstration mission is designed to address the unique needs of deep space navigation[25], but given the clock's low size, mass and power, it is also well suited for GNSS applications in Earth orbit. The DSAC payload, consisting of a trapped-ion

[1]Jet Propulsion Laboratory, California Institute of Technology, Pasadena, CA, USA. [2]These authors contributed equally: Eric A. Burt, John D. Prestage, Robert L. Tjoelker.
✉e-mail: eric.a.burt@jpl.nasa.gov

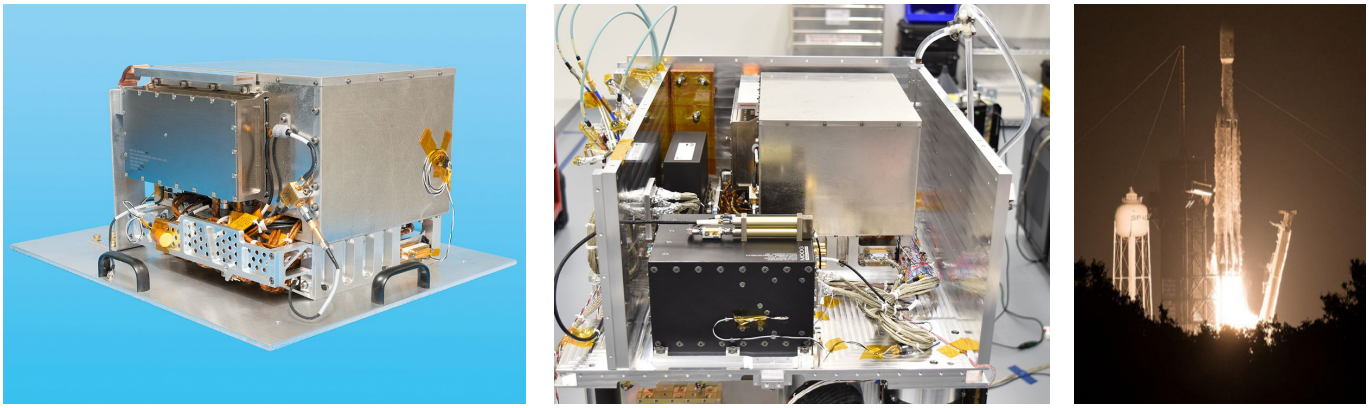

Fig. 1 | The Deep Space Atomic Clock launch. Left to right: the DSAC clock (credit: JPL); the DSAC instrument, including GPS receiver and ultrastable oscillator (USO), integrated in the spacecraft payload (credit: General Atomics); and the launch of Space-X Falcon Heavy STP-2 carrying DSAC into space (credit: NASA).

clock and its 1×10^{-13} class ultrastable local oscillator (LO) together with a Global Positioning System (GPS) receiver to aid comparisons with clocks on the ground, was launched in June 2019 aboard the General Atomics' Orbital Test Bed spacecraft into a 720-km, 100-min Earth orbit (Fig. 1) and first powered on in space in August 2019. The 2-year DSAC mission is designed to demonstrate clock operability, characterize performance of the technology in space and carry out several navigation experiments to demonstrate its utility in that domain.

DSAC trapped-ion clock

The DSAC ion clock, payload configuration and ground testing, as well as its navigational uses and some scientific applications, have been previously described[14,26]. Here we summarize these and then focus on results obtained after launch.

At the heart of the DSAC clock are two linear radiofrequency Paul ion traps[27,28], one having four rods (the quadrupole or load trap), the other having sixteen rods (the multipole trap). Figure 2 shows a schematic cross-section of the vacuum chamber, revealing the traps. A radiofrequency voltage is applied across alternating trap rod pairs, with the field strength decreasing linearly towards the trap axis. Ions seek the weakest field and are thereby trapped in the centre. The other two images in Fig. 2 show contour plots of field strength for the load trap and multipole trap in a plane perpendicular to this axis. In the load trap, the non-zero time-average force on the ions from strong field to weak field regions gives rise to an effective quadratic potential proportional to E^2, where E is the electric field magnitude. Ions in the trapping region execute oscillatory motion at about 50 kHz in the radial direction (axially, ions are confined by d.c. voltage endcaps and move ballistically). The DSAC clock confines a cloud of up to 10^7 ions. The inward trapping force is partially balanced by Coulomb repulsion pushing ions outwards. As a result, the ion cloud occupies a region that extends radially about 1 mm, such that the spatial- and ensemble-averaged radiofrequency field experienced by the trapped ions is non-zero. This region of confinement is smaller than the interrogation wavelength, so the first-order Doppler shift, proportional to $-v/c$ (where v is ion velocity and c is the speed of light), is eliminated[29]. While $\langle v \rangle = 0$ for trapped ions, $\langle v^2 \rangle$ is of order 10^5 m^2 s^{-2}, resulting in a relativistic second-order

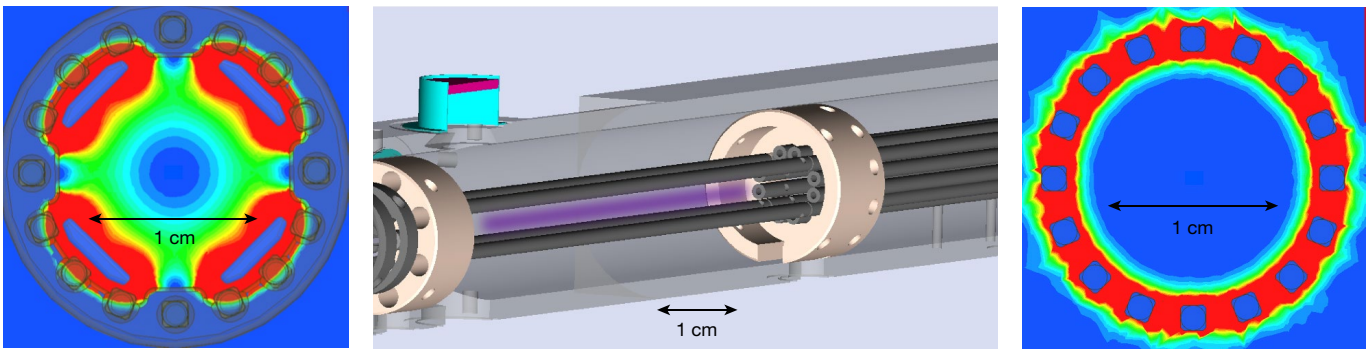

Fig. 2 | Clock vacuum chamber and traps. The centre image is a cross-section schematic of a DSAC-like vacuum chamber (light grey), showing the trap rods for the load trap used to initially load ions, prepare their initial internal state and read out their final state (on the left in the centre image) and for the multipole trap (dark grey on the right in the centre image) where sensitive microwave interrogation of the clock transition occurs. The optical window assemblies where state preparation light is brought in and signal light is detected are shown in cyan and magenta. A representation of the trapped-ion cloud lying on the load trap axis is shown in purple. The image on the left shows a contour plot of the amplitude of the quadrupole radiofrequency field applied to the load trap rods in a plane perpendicular to the rods. Dark blue corresponds to low field and red to high field. The four symmetric blue rectangles correspond to the trap rods. Ions are 'weak-field seeking', so the blue circle in the centre is the low-field region where the ions are trapped. Ions experience a radiofrequency amplitude that varies with the radial distance from the centre. In addition to thermal motion, ions oscillate at the trap radiofrequency, a process called 'micro-motion' that results in a second-order Doppler frequency shift in the clock transition. The image on the right shows a contour plot of the radiofrequency field amplitude in the multipole trap with the same colour designations. Note that the centre trapping region in the multipole trap (dark blue) corresponds to a considerably larger fraction of the volume inside the trap rods than for the load trap. This is representative of its near square-well potential. In the multipole trap, ions move quasi-ballistically with very little micro-motion until they come close to the trap rods, such that the time-averaged micro-motion and second-order Doppler shift are much smaller in the multipole trap.

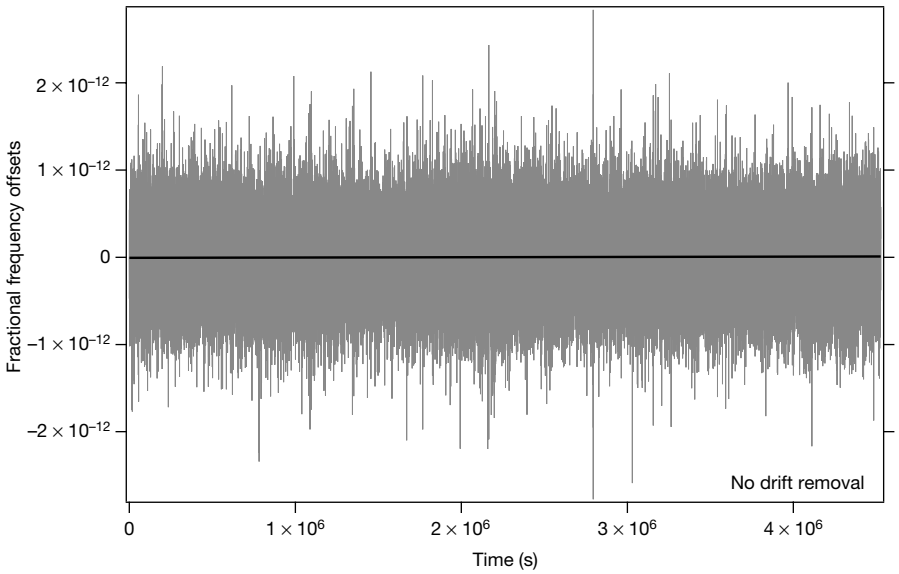

Fig. 3 | Clock frequency offsets in space. Frequency offsets versus time of the DSAC instrument in space relative to the USNO master clock, which is a hydrogen maser steered to UTC. In these data, DSAC is operating in the re-purposed load trap. The black line is a least-squares fit to a straight line, which shows a drift of $+3.0(0.7) \times 10^{-16}$ per day, an order of magnitude lower than other space clocks.

Doppler shift of about 1×10^{-12} in the load trap. The main advantage of the multipole trap is that the radial potential created by this configuration approaches that of a square well (see the contour plot on the right side of Fig. 2). Ions in the multipole trap experience a lower $\langle E^2 \rangle$ than in the load trap, which results in a lower $\langle v^2 \rangle$ and virtually eliminates the ion-number-dependent second-order Doppler shifts, a primary systematic effect in the clock[28].

To construct a clock based on the frequency associated with the difference between quantized atomic energy levels, a synthesized frequency referenced to an LO is used to interrogate the atoms or ions (see 'Clock operation sequence' in Methods). In the case of Hg^+, this is 40.5 GHz driving the $S_{1/2}, F = 0, m_F = 0$ to $S_{1/2}, F = 1, m_F = 0$ magnetic-field-insensitive hyperfine clock transition (see Extended Data Fig. 2). If the synthesized LO frequency is correct, the atomic response ('signal') will be large, otherwise it will be small. This response is used to form a correction that is fed back to the LO, thereby closing the loop and transferring the atomic energy-level stability to the output of the LO (DSAC actually uses a more complex LO architecture)[30]. A 194-nm light source is used to prepare the initial state of the ions and to read out the state after microwave interrogation (see 'Clock operation sequence' in Methods for details).

Collisions with a neon buffer gas keep trapped ions near room temperature so that thermal excitations do not eject them from the trap. During DSAC clock testing, a small neon depletion mechanism was discovered, which rendered clock operation in the multipole trap no longer viable[14]. Although operation in the load trap was still possible, the quadrupole load trap design in this version of the clock is not optimized for clock operation. As a result, neither the short-term nor the long-term stability in the load trap will be as good as is possible in the multipole trap, but long-term stability in the load trap was still more than sufficient to satisfy the mission requirement of 2×10^{-14} at one day, and load-trap-based clock operation has been the primary mission configuration. On the ground, the DSAC clock demonstrated a stability of $2 \times 10^{-13}/\tau^{1/2}$ operating in the multipole trap with a maser as the LO and a stability of 2×10^{-15} at one day[14].

Clock operation in space

Before running the clock continuously, it was thoroughly characterized in the space environment. The largest frequency shifts in the DSAC clock are due to magnetic effects, ion-number-dependent relativistic Doppler effects, and the effects of background gas collisions. Overall sensitivity to temperature changes, including electronic sensitivities, enters through these three fundamental paths. Here we only summarize these characterizations. See the Methods section for details on how each measurement was made.

During each orbit, the magnetic field has a peak-to-peak variation of about 25 μT, over 100 times as much as in a typical laboratory setting. The combination of the low sensitivity of the Hg^+ clock transition to magnetic shifts (about 4 times lower than caesium, for example) and the three layers of magnetic shielding reduce associated frequency shifts to below the clock noise at the orbital period time. Variations in the clock frequency due to trace gas evolution are expected to be low (see 'Background pressure evolution' in Methods). In part, this is due to the high-temperature bakeout applied during clock preparation. Measurements placed a limit on frequency variations due to this effect of well below 1×10^{-15} on a day timescale. Residual relativistic second-order Doppler effects in the load trap depend primarily on the number of ions trapped. The total effect is about −50 mHz (about -1×10^{-12}) from an empty to full trap (see 'Thermal and Doppler effects' in Methods). Therefore, an ion number stability of 0.1% is required to support clock stability at the 10^{-15} level. This level of ion number stability is normally achieved after ion loading equilibrates with the residual trap loss mechanisms. The total temperature sensitivity of the DSAC instrument is a combination of several factors, including relativistic Doppler effects, electronics sensitivities, and stray temperature-dependent magnetic effects that have not yet been fully characterized (hereafter we will reserve 'total temperature sensitivity' to refer to this combination). When it was possible to disentangle these, the fundamental sensitivity of the clock was measured to be as low as $-2.3(1.1) \times 10^{-15}$ °C^{-1} with no active thermal stabilization on the ion portion of the clock or electronics (the LO is temperature-stabilized, but this only affects short-term performance). This point is notable, as rarely, if ever, are space clocks able to operate without some form of temperature control.

Orbital transits through South Atlantic Anomaly expose the clock to a high radiation environment. This results in increased photomultiplier tube (PMT) counts and small changes in the LO frequency drift rate, but the DSAC control algorithm is designed to filter these out, so there is no observed impact on clock output (see Methods).

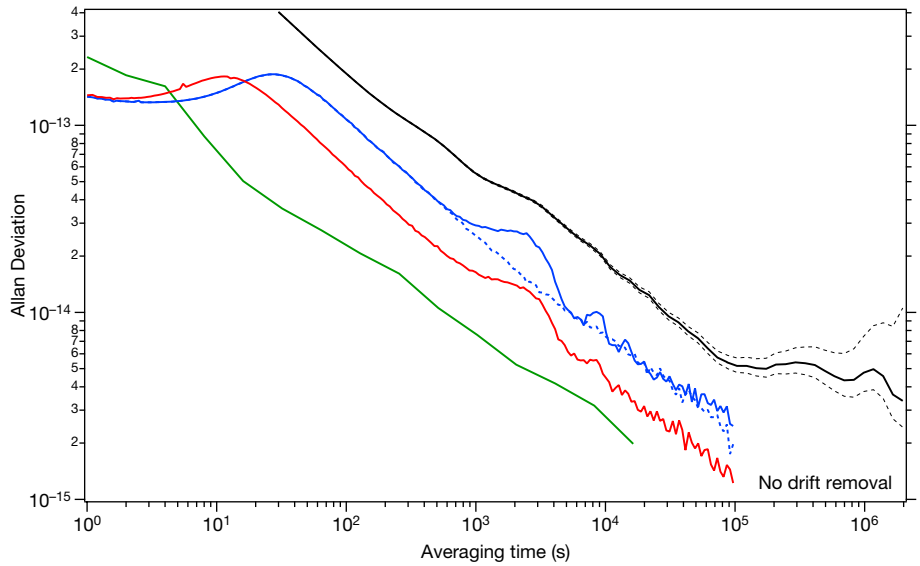

Fig. 4 | Clock stability in space. Allan deviation of the DSAC clock relative to the USNO master clock (including GPS measurement system noise) while operating in the repurposed load trap (solid black line, with dashed black lines indicating 68% confidence intervals). The USNO master clock is a hydrogen maser periodically steered to UTC. The low Allan deviation at long times is indicative of very low drift and demonstrates the applicability of DSAC technology to applications requiring autonomy, such as GNSS and deep space navigation. Temperature servo loops that control the lamp and getter temperatures were not necessary and were disabled, so that the data shown are with no active thermal control. Also shown is a simulation of expected clock performances including USO noise, aliasing, control loop effects and ion clock signal noise as well as environmental perturbations[30] with environmental disturbances at the orbital period (solid blue) and without (dashed blue). The difference between the blue and black lines shows that the black line is measurement-system limited for averaging times less than a day (about 86,000 s). Clock operation parameters used here were not fully optimized. A simulation of expected clock performance with more optimal parameters is shown in red. For comparison, the green trace shows operation achieved on the ground with the optimized multipole trap and a hydrogen maser acting as the LO. Operation with a maser LO reduces control loop noise in the short term and aliasing noise[33] on medium to long timescale (the 1-s value is degraded by the 20-MHz user output synthesizer; Extended Data Fig. 1), but even with a crystal LO, operation in the multipole trap would have resulted in better performance than shown in the red trace. Note that the black trace is an overlapping Allan deviation, while all other traces are non-overlapping.

Clock performance in space

At clock start up, the LO frequency can be far off the correct value, and it must be put on frequency before the clock can function normally—a process called LO acquisition[22]. Once the LO is acquired, the clock requires about 12 h to reach thermal equilibrium. During this time, the trapped-ion number also slowly approaches its equilibrium value. The expected short-term performance for the clock operating in the repurposed load trap is $7\times10^{-13}/\tau^{1/2}$ greater than the instability achieved in the optimized multipole trap, but still below the flight measurement system noise (see 'Stability measurement system noise: GPS' in Methods), for averaging times of less than a day. For all averaging times, the measurement system places at least an upper bound on clock performance[31].

Figure 3 shows 52 days of continuous frequency offsets for the DSAC clock relative to the USNO master clock using GPS. Frequency offsets include both clock noise and GPS measurement system noise. The USNO master clock consists of a hydrogen maser at the US Naval Observatory that is steered to Coordinated Universal Time (UTC). For 4 days of the data, when the USNO clock was not available, the reference clock from the Royal Observatory of Belgium was used instead (see Methods). Clock drift is estimated using a linear least-squares fit to the non-drift-removed frequency offsets from the reference, which gives a slope of $+3.0(0.7)\times10^{-16}$ per day.

Figure 4 shows the measured Allan deviation[32] for the same run. The deviation from white frequency noise (proportional to $1/\tau^{1/2}$) after 10^5 s is consistent with slow thermal effects related to variations in the host spacecraft orientation relative to the Sun (see Methods) but can also be caused by the reference clock instability. The flicker noise floor of the clock and measurement system is not known, so flicker noise may also contribute on these timescales. A frequency stability of 3×10^{-15} corresponding to a time deviation of less than 4 ns is shown at 23 days (about 2×10^6 s). Over many separate runs, the clock stability at one day varied between 3×10^{-15} and 5×10^{-15}, depending on the temperature variations for a given run. In addition to being taken in the lower-performing load trap, this performance level is even more notable because the data were taken without temperature control of the ion trap and associated electronics during a time when the baseplate temperature varied by 9 °C. It is important to note that the noise floor of the measurement system is not precisely known for operation in space where one platform is moving and is exposed to a wide-ranging thermal environment, but it is possible that it is contributing at the level of the long-term performance observed (see 'The stability measurement system: GPS' in Methods). Thus, the measurements stated here contain noise from the clocks on either end of the comparison as well as from the measurement system and so are an upper bound for the DSAC clock alone[31]. This long-term performance, already more than an order of magnitude better than existing space clocks, will enable one-way navigation, allowing control of deep space satellites in near real-time[18] as well as new planetary science measurements[26].

Conclusions

We have demonstrated a trapped-ion atomic clock operating in space. Clock operation was fully characterized over a 9-month period, and long-term operation will continue through the remainder of the 2-year mission. On the ground, the clock's short-term stability measured in the multipole trap of the two-trap system was between 1×10^{-13} and 2×10^{-13} at 1 second and $2\times10^{-13}/\tau^{1/2}$, and in space the short-term stability in the repurposed load trap was estimated to be $7\times10^{-13}/\tau^{1/2}$. In space, a stability of 3×10^{-15} to 5×10^{-15} was measured at 1 day, and 3×10^{-15} (no drift removal) was measured at 23 days, equivalent to a time deviation of less than 4 ns. In addition, an uncorrected drift rate of $+3.0(0.7)\times10^{-16}$

per day was also observed, demonstrating this technology's utility for applications requiring autonomous operation. Both long-term observations were made in the presence of a 9 °C variation in temperature and no temperature control on the ion trap and associated electronics. With clock sensitivities to environmental effects measured on the ground, operation in the more extreme environment of space was observed. In all cases, clock frequency shifts due to orbital environmental effects were near or below the noise floor of the measurement system and that of the estimated Allan deviation of the clock itself. Radiation effects due to orbital passes through the South Atlantic Anomaly were also studied and found not to limit clock operation. Work is in progress to extend the lifetime of this technology past the current expected 3–5 years, out to 10 years or more. These efforts will be focused on the ultraviolet light source and the vacuum chamber pressure, including the buffer gas and mercury vapour partial pressures. Infusion of this technology into future space-flight missions is currently being explored, with likely applications to one-way navigation and planetary science.

Online content

Any methods, additional references, Nature Research reporting summaries, source data, extended data, supplementary information, acknowledgements, peer review information; details of author contributions and competing interests; and statements of data and code availability are available at https://doi.org/10.1038/s41586-021-03571-7.

1. Thornton, C. L. & Border, J. S. *Radiometric Tracking Techniques for Deep-Space Navigation* (Wiley-Interscience, 2003).
2. Mallette, L. A., White, J. & Rochat, P. Space qualified frequency sources (clocks) for current and future GNSS applications. *IEEE/ION Position Locat. Navig. Symp. (Online)*, https://doi.org/10.1109/PLANS.2010.5507225 (2010).
3. Prestage, J. D., Tjoelker, R. L. & Maleki, L. Atomic clocks and variations of the fine structure constant. *Phys. Rev. Lett*. **74**, 3511 (1995).
4. Safronova, M. S. The search for variation of fundamental constants with clocks. *Ann. Phys*. **531**, 1800364 (2019).
5. McGrew, D. et al. Atomic clock performance enabling geodesy below the centimetre level. *Nature* **564**, 87 (2018).
6. Hees, A., Guéna, J., Abgrall, M., Bize, S. & Wolf, P. Searching for an oscillating massive scalar field as a dark matter candidate using atomic hyperfine frequency comparisons. *Phys. Rev. Lett*. **117**, 061301 (2016).
7. Vessot, R. F. C. et al. Test of relativistic gravitation with a space-borne hydrogen maser. *Phys. Rev. Lett*. **45**, 2081 (1980).
8. Prestage, J. D., Dick, G. J. & Maleki, L. Linear ion trap based atomic frequency standard. *IEEE Trans. Instrum. Meas*. **40**, 132 (1991).
9. Cutler, L. S., Giffard, R. P. & McGuire, M. D. A trapped mercury 199 ion frequency standard. In *Proc. 13th Annual Precise Time and Time Interval (PTTI) Applications and Planning Meeting*, 563–577 (Institute of Navigation, 1981).
10. Tjoelker, R. L. et al. A mercury ion frequency standard engineering prototype for the NASA deep space network. In *Proc. 50th IEEE International Frequency Control Symposium*, 1073–1081 (IEEE, 1996).
11. Burt, E. A., Diener, W. A. & Tjoelker, R. L. A compensated multi-pole linear ion trap mercury frequency standard for ultra-stable timekeeping. *IEEE Trans. Ultrason. Ferroelectr. Freq. Control* **55**, 2586 (2008).
12. Hinkley, N. et al. An atomic clock with 10^{-18} instability. *Science* **341**, 1215 (2013).
13. Brewer, S. M. et al. $^{27}Al^{+}$ quantum-logic clock with a systematic uncertainty below 10^{-18}. *Phys. Rev. Lett*. **123**, 033201 (2019).
14. Tjoelker, R. L. et al. Deep Space Atomic Clock (DSAC) for a NASA Technology Demonstration Mission. *IEEE Trans. Ultrason. Ferroelectr. Freq. Control* **63**, 1034–1043 (2016).
15. Lutwak, R., Emmons, D., Garvey, R. M. & Vlitas, P. Optically pumped cesium-beam frequency standard for GPS-III. In *Proc. 33rd Annual Precise Time and Time Interval (PTTI) Applications and Planning Meeting*, 19–30 (Institute of Navigation, 2001).
16. Riley, W. J. Rubidium atomic frequency standards for GPS block IIR. In *Proc. 22nd Annual Precise Time and Time Interval (PTTI)*, 221–230 (Institute of Navigation, 1990).
17. Droz, F. et al. Space passive hydrogen maser—performances and lifetime data. In *Proc. 2009 IEEE International Frequency Control Symposium Joint with the 22nd European Frequency and Time Forum*, 393–398 (IEEE, 2009).
18. Seubert, J., Ely, T. & Stuart, J. Results of the deep space atomic clock deep space navigation analog experiment. In *Proc. AAS/AIAA Astrodynamics Specialist Conference* (American Astronomical Society, in the press).
19. Codik, A. Autonomous navigation of GPS satellites: a challenge for the future. *J. Inst. Navig*. **32**, 221–232 (1985).
20. Dehmelt, H. G. Monoion oscillator as potential ultimate laser frequency standard. *IEEE Trans. Instrum. Meas*. **IM-31**, 83–87 (1982).
21. Liu, L. et al. In-orbit operation of an atomic clock based on laser-cooled ^{87}Rb atoms. *Nat. Commun*. **9**, 2760 (2018).
22. Tjoelker, R. L. et al. Mercury atomic frequency standards for space-based navigation and timekeeping. In *Proc. 43rd annual Precise Time and Time Interval (PTTI) Systems and Applications Meeting*, 209–304 (Institute of Navigation, 2011).
23. Prestage, J.D., Chung, S., Le, T., Lim, L., and Maleki, L. Liter sized ion clock with 10^{-15} stability. In *Proc. Joint IEEE IFCS and PTTI*, 472–476 (IEEE, 2005).
24. Prestage, J. D. & Weaver, G. L. Atomic clocks and oscillators for deep-space navigation and radio science. *Proc. IEEE* **95**, 2235–2247 (2007).
25. Ely, T. A., Seubert, J. & Bell, J. in *Space Operations: Innovations, Inventions, and Discoveries*, 105–138 (American Institute of Aeronautics and Astronautics, Inc., 2015).
26. Ely, T. A., Burt, E. A., Prestage, J. D., Seubert, J. M. & Tjoelker, R. L. Using the Deep Space Atomic Clock for navigation and science. *IEEE Trans. Ultrason. Ferroelectr. Freq. Control* **65**, 950–961 (2018).
27. Prestage, J. D., Dick, G. J. & Maleki, L. New ion trap for frequency standard applications. *J. Appl. Phys*. **66**, 1013 (1989).
28. Prestage, J. D., Tjoelker, R. L. & Maleki, L. Higher pole linear traps for atomic clock applications. In *Proc. 1999 Joint European Frequency and Time Forum and IEEE International Frequency Control Symposium*, 121–124 (IEEE< 1999).
29. Dicke, R. H. The effect of collisions upon the Doppler width of spectral lines. *Phys. Rev*. **89**, 472 (1953).
30. Enzer, D., Diener, W., Murphy, D., Rao, S. & Tjoelker, R. L. Drifts and environmental disturbances in atomic clock subsystem: quantifying local oscillator, control loop, & ion resonance interactions. *IEEE Trans. Ultrason. Ferroelectr. Freq. Control* **64**, 623–633 (2017).
31. Ely, T. A., Murphy, D., Seubert, J., Bell, J. & Kuang, D. Expected performance of the Deep Space Atomic Clock Mission. In *Proc. AAS/AIAA Space Flight Mechanics Meeting*, 807–826 (American Astronomical Society, 2014).
32. Howe, D. A., Allan, D. W. & Barnes, J. A. Properties of signal sources and measurement methods. In *Proc. 35th Annual IEEE Symposium on Frequency Control*, 1–47 (IEEE, 1981).
33. Dick, G. J. Local oscillator induced instabilities in trapped ion frequency standards. In *Proc. 19th Precise Time and Time Interval Symposium*, 133–147 (Institute of Navigation, 1987).

Methods

Clock operation sequence

Extended Data Fig. 1 shows a system-level block diagram of the DSAC payload. A 1×10^{-13} class USO serves as the LO providing 10 MHz to the DSAC 40.5-GHz synthesizer that generates the clock frequency and to a user output synthesizer at 20.456 MHz used as the reference for the GPS receiver. The 40.5-GHz microwave signal is directed to the ion system via a Ka-band waveguide and a Ka-band horn to interrogate the trapped ions. The trap is enclosed in an ultrahigh-vacuum system that is surrounded by three mu-metal magnetic shields. Also attached to the ion subsystem is the ultraviolet light subsystem, which consists of the plasma discharge lamp (as ultraviolet light source), optics and a PMT detector. The plasma discharge lamp is electrodeless, consisting of a fused silica envelope surrounded by a coil resonator. The trapped ions used in the clock are $^{199}Hg^{+}$, but the lamp plasma is comprised of $^{202}Hg^{+}$, which has a spectral line resonant with the $S_{1/2}, F=1$ to $P_{1/2}, F=1$ transition, but not the $S_{1/2}, F=0$ to $P_{1/2}, F=1$ transition (see the level diagram in the next section). Thus, the discharge light can be used to optically pump $^{199}Hg^{+}$ clock ions into the $F=0$ ground state. After microwave interrogation from the $S_{1/2}, F=0$ to $S_{1/2}, F=1$, the same discharge light can be used for state detection: if the microwave frequency were on resonance with the clock transition, $^{199}Hg^{+}$ ions that were pumped into the $S_{1/2}, F=0$ state would make the transition to the $S_{1/2}, F=1$ state and would be resonant with the discharge light, resulting in a detectable fluorescence signal. Otherwise, they will stay in the $F=0$ state, producing no fluorescence. The detected fluorescence is directed to the clock controller where software determines each frequency correction to be applied to the 40.5-GHz clock synthesizer and the user output synthesizer.

The ultrahigh-vacuum chamber includes a quadrupole load trap where ions are loaded and prepared, and a multipole trap where atom interrogation is performed. The DSAC clock also allows for atom interrogation and full clock operation to take place in the load trap, though at a reduced performance level. Ions are loaded into the trap from a background neutral mercury vapour ionized by electrons from a heated LaB_6 filament held at a negative high voltage relative to the trap region. Clock electronics include radiofrequency drivers for the two traps, an electron emitter driver, the clock controller, and a stable current source that drives coils surrounding the vacuum chamber to establish the clock quantization axis. The ultraviolet light source is enclosed in a hermetically sealed O_2 back-filled cell. Bias fields (d.c.) are applied to the load trap and multipole trap rods to affect transfer ('shuttling') of ions between the two traps. All telemetry, including clock signal counts, background counts, frequency corrections and many temperatures, is relayed to the ground daily.

Atomic energy-level diagram

Extended Data Fig. 2 shows the ^{199}Hg(II) level structure along with the various transitions used in the clock. The $S_{1/2}, F=0, m_F=0$ to $S_{1/2}, F=1, m_F=0$ field-insensitive hyperfine transition forms the basis of the clock. It is optimally driven by a microwave field at 40.5 GHz polarized parallel to the quantization axis. In DSAC, the microwave launcher establishes a field that is at 45° relative to this axis, so it has a component both perpendicular and parallel. The perpendicular component can be used to drive the magnetically sensitive neighbouring lines for diagnostic purposes, but during normal clock operation these lines are detuned 140 kHz and do not perturb the clock. The $S_{1/2}, F=1$ to $P_{1/2}, F=1$ optical transition is driven by the plasma discharge source just described at 194 nm and is used to optically pump ions into the initial state and to read out the state after microwave interrogation.

The stability measurement system: GPS

It is possible to determine most of the clock performance characteristics from its own telemetry. For instance, with a knowledge of the signal-to-noise ratio (SNR) and atomic line Q of the clock transition, along with clock operation parameters, one can determine its short-term stability directly by using:

$$\sigma_y(\tau)=\frac{1}{\pi\,\mathrm{SNR}_{1/2}\,Q}\sqrt{\frac{t_c}{\tau}} \tag{1}$$

where τ is the averaging time, t_c is the clock cycle time, $\mathrm{SNR}_{1/2}$ is the signal-to-noise ratio at the half-height of the resonance line, and $Q=f_0/\Delta f$ where f_0 is the ion resonance frequency and Δf is the full-width at half-maximum (FWHM) of the resonance line shape. A more complete description of the expected Allan deviation would need to include aliasing noise[33], which depends on the level of LO noise and the particular clock cycle used. Modelling indicates that this noise term contributes $5\times10^{-13}/\tau^{1/2}$ for the LO noise and clock parameters used during the runs presented in this paper. If aliasing is a white frequency noise process, it can be added appropriately with expression (1). $\mathrm{SNR}_{1/2}$ is easily estimated using the periodically measured resonance signal size and by assuming shot-noise-limited performance on the detection system. The Q is determined by the known resonance frequency and the interrogation time (Rabi time), which determines the FWHM. In the repurposed load trap used for the space demonstration, with $t_c=12.5$ s, $f_0=40.5$ GHz, $\mathrm{SNR}_{1/2}=23$ and a Rabi interrogation time of 2 s, the estimated short-term stability is $7\times10^{-13}/\tau^{1/2}$ (including aliasing noise[33]). However, to determine the clock's long-term stability requires a comparison to a second clock that is more stable on the timescale of interest. Rather than carry a second clock on board the spacecraft, the DSAC payload includes a GPS receiver providing both code and carrier phase measurements, thereby enabling high-precision GPS frequency transfer[34] between DSAC and any clock on the ground also connected to a GPS receiver, in particular those providing a realization of UTC.

To process GPS data, we use the GIPSY-OASIS code to undertake 30-h arc precise point positioning with ambiguity resolution[35]. This determines the offset $x(t)$ in coordinate time between the DSAC clock and the reference clock used in JPL's rapid orbit and clock products. Subsequently we convert these 30-h $x(t)$ datasets to 24-h daily $x(t)$ datasets. After this, we convert $x(t)$ to proper time using the method described next for a dataset that can span any time range, typically many days. In principle, this enables comparison to the most stable clocks in the world, as all national metrology laboratories use this method. However, compared with conventional GPS frequency comparisons, our measurement system must contend with several additional challenges such as the low-Earth-orbit motion of one platform and an uncontrolled GPS receiver thermal environment. Studies of these and other factors have shown[31] that, relative to the clock, our measurement system has a higher noise level in the short term.

For averaging times greater than a day, it is possible to achieve a measurement system stability below 10^{-15} using GPS frequency transfer[36]. We have not done a thorough analysis of long-term noise for our measurement system in particular. Given the orbital considerations, together with the fact that the reference clock is a hydrogen maser, it is likely that measurement system noise for long averaging times is above 10^{-15} and therefore may contribute to estimated clock noise on these timescales as well. For averaging times for which the noise of the DSAC clock is below the measurement noise floor, it is only possible to place an upper bound on clock stability performance.

To perform the clock comparison, the GPS receiver must be carefully configured for operation in space. In particular, for the DSAC mission, it was necessary to calibrate the carrier phase and pseudo-range measurements for the receiver's temperature sensitivity. In addition, DSAC telemetry must be corrected for relativistic variations: the gravitational redshift and Doppler shifts. To aid each comparison, the receiver is dynamically transformed to the geoid[37] by using the following equation:

$$\tau_s=\int \mathrm{d}t\left[1+\frac{\Phi(r)-\Phi_0}{c^2}-\frac{v^2}{2c^2}\right] \tag{2}$$

where τ_s is the spacecraft proper time, $\Phi(r)$ is the Newtonian gravitational potential at radius r from the geoid, Φ_0 is the gravitational potential on the Earth's geoid, c is the speed of light and v is the speed of the spacecraft in the Earth-centred inertial reference frame.

Furthermore, to obtain accurate solutions, the second-order terms in a multipole expansion of the gravitational potential must be retained so that

$$\Phi(r) = -\frac{GM}{r}\left[1 - J_2\left(\frac{a_1}{r}\right)^2 \frac{(3z^2 - r^2)}{2r^2}\right] \quad (3)$$

where J_2 parameterizes the quadrupole contribution to the gravitational potential, a_1 is the equatorial radius of the Earth and z is the third Cartesian component of the position vector $\mathbf{r}$. Without the additional J_2 terms in the potential, clock comparisons to the ground are limited by GPS errors. This was also demonstrated on the GRACE satellites as described in ref. [37].

A careful analysis of expected DSAC measurement system noise was carried out[31] that characterized the impact of the known error sources. The most important of these include: GPS measurement noise, GPS orbit and clock estimate errors, multipath errors, instabilities in the ground reference clock, and thermal calibration errors of the GPS receiver phase. Also included, but not as important, were uncertainties in modelling spacecraft drag accelerations, spacecraft solar pressure accelerations, and the phase centre knowledge of the GPS antenna with respect to the spacecraft centre of mass. Extended Data Fig. 3 shows the measured overlapping Allan deviation with and without corrections for relativistic and GPS receiver thermal effects. Also superimposed is the simulated expected clock performance up to a day of averaging with the clock parameters used during the run, with and without effects from orbital thermal and magnetic disturbances.

As shown in Extended Data Fig. 3, measurement system noise is about twice as large as the expected clock performance in the short term. For averaging times greater than a day, clock environmental effects are expected to contribute near the level of the black line. As described earlier in this section, measurement system noise may also contribute near this level for these averaging times. Therefore, the data shown can only be taken as an upper bound on actual clock performance.

Magnetic effects

An environmental aspect that must be managed by most space clocks is variations in the ambient magnetic field. The quantization axis of the DSAC clock is determined by a coil inside the magnetic shields and a stable current source that generates a field of about 10 μT. The stability of this current source is at the 10 ppm level, resulting in random field variations of 0.1 nT and clock variations due to this internal current source noise well under 10^{-15}. Sensitivity to external magnetic variations is reduced by three-layer mu-metal shielding. The sensitivity due to external magnetic field variations in the weakest shielding direction around the load trap was measured on the ground to be 7×10^{-16} μT^{-1}. (The sensitivity in the optimized multipole trap region is over an order of magnitude smaller.)

At the DSAC orbit of approximately 720 km, the clock sees variations in Earth's magnetic field of 25 μT, a range that is over 100 times the variation typically seen in the laboratory. There are three mitigating factors that reduce the effects of these large magnetic field variations for the DSAC clock: (1) at an atomic response of 9.7 mHz μT^{-2}, the mercury clock transition has a very low sensitivity to magnetic variations (about 4 times lower than caesium, for example); (2) the use of high-performance magnetic shielding with a shielding effectiveness of up to 20,000 (although not as good in the load trap at only about 5,000, owing to shield holes to accommodate optics); and (3) the variations occur at the orbital period of about 6,000 s, at which time their contribution to the clock Allan deviation is below the noise floor of the clock. Extended Data Fig. 4 shows magnetic field variations near the clock as a function of time, as measured by a magnetometer on the spacecraft. In the graph, the component of the field in the weakest shielding direction is shown. Extended Data Fig. 5 shows the simulated Allan deviation of frequency shifts calculated in the worst case (weakest shielding direction always aligned with maximum field direction) from the measured field variations. Superimposed is the expected DSAC clock noise floor for operation in the multipole trap without LO aliasing effects[33] ($2 \times 10^{-13}/\tau^{1/2}$) and for the load trap ($7 \times 10^{-13}/\tau^{1/2}$). For both modes of operation, the magnetic effect (assuming the worst-case magnetic shielding direction) is just at, or is below, the noise floor.

Thermal and Doppler effects

During pre-launch evaluations, it is usually possible to vary one parameter while holding others constant. In space, this is rarely possible. The overall thermal sensitivity of the clock and the sensitivity to variations in the number of ions trapped—the number-dependent second-order Doppler effect $df/f = -v^2/(2c^2)$—are an example of effects that are difficult to decouple. For the latter, as the ion cloud changes size, the time-averaged trap radiofrequency field amplitude as seen by the ions varies, leading to changes in the ensemble-averaged ion velocity v and the second-order Doppler shift[38]. Over a particular 4-day period, the clock temperature varied by about 5 °C, and the number of trapped ions was intentionally varied by about 50% with the electron emitter turned off. The frequency shift coefficients due to these are easily separated by exploiting the different functional forms of their variation (one was monotonic while the other was not). With the large change in trapped-ion number here, the change in the associated second-order Doppler effect dominates temperature-related effects. The trapped-ion number is not known directly but is approximately proportional to clock signal size. Clock signal size is determined by periodically interrupting clock operation to take the difference between the clock signal fluorescence on resonance and off. Individual signal size measurements are usually shot-noise-limited in the total number of PMT counts, which includes background light in addition to clock signal fluorescence. However, long-term variations in lamp output due to temperature changes will cause variations in this metric that are independent of ion number. Thus, the signal size can only be used to represent the ion number during times when the lamp temperature is stable or by adjusting the signal size to account for the known impact of temperature on lamp output. Extended Data Fig. 6 shows a least-squares second-order polynomial fit of frequency offsets plotted against signal size. Theoretically, the dependence should be linear, and the deviation from linearity at higher signal sizes shown is due to larger ion clouds extending beyond the optical interrogation region. Larger ion clouds are also subject to additional radiofrequency heating. Thus, the linear component of the fit, effectively extrapolating back to an empty trap, gives the most reliable representation of the second-order Doppler shift coefficient. In experimental units, this is $-5.6(1.2) \times 10^{-17}$ per PMT count of clock signal size. For a current clock signal of 22,000 counts, this corresponds to a total effect of about -1×10^{-12} from an empty to full trap. To maintain 1×10^{-15} stability at a day requires constraining the trapped-ion number to a fraction of a per cent.

The residuals to the polynomial fit used to obtain the Doppler sensitivity have a systematic trend correlated with the variation in temperature, which was not monotonic. When the fit residuals are plotted against the temperature, a linear trend is apparent (see Extended Data Fig. 7). The linear slope gives the total temperature sensitivity (as in the main text, we reserve the term 'total temperature sensitivity' of the clock to indicate the combination of relativistic Doppler effects, electronics sensitivities and stray temperature-dependent magnetic effects) in this case as $-2.3(1.1) \times 10^{-15}$ °C^{-1}. This is close to the thermal Doppler limit[39] and demonstrates how this technology is able to achieve a high level of stability in a varying thermal environment, even with no temperature control.

The most important thermal variations occur at the orbital period of 6,000 s, but there are other thermal timescales as well. For instance, on a roughly daily cadence, the orbital ground track passes over regions that have different albedos, such as the Sahara Desert. Another temperature variation at an approximate daily period comes from certain spacecraft housekeeping activities. These can require an increase in spacecraft power consumption, which leads to variations in the spacecraft temperature. Finally, the solar illumination of the spacecraft varies on a roughly month timescale as the solar elevation angle, or beta angle, with respect to the orbital plane changes (the beta angle is defined as the angle between a line from the Earth to the Sun and the orbital plane.) This combined with occasional spacecraft re-orientations to keep the main spacecraft radiator in shadow leads to an approximate 17-day period in the temperature as seen by the ions in this dataset. Extended Data Fig. 8 shows the temperature in the load trap, the most relevant temperature for current clock operation, as a function of time.

The DSAC demonstration mission currently operates with no thermal control. The instrument internal temperature floats with the changing environment and lags with a several hour time constant. Extended Data Fig. 8a shows 52 days of data and an overall approximately periodic temperature trend associated with the variation in the spacecraft beta angle. The average peak-to-peak variation is about 4 °C with an average period of about 17 days. Extended Data Fig. 8b is a 5-day subset and shows an approximate daily sinusoid in temperature with a peak-to-peak variation of 0.5 °C. Finally, Extended Data Fig. 8c is a 1-day subset showing the orbital effect with a peak-to-peak variation of about 0.3 °C. The total temperature sensitivity of the measurement is due to a combination of several factors, not all of which are constant over time or fundamental to the technology. In addition to the ions themselves, these effects include temperature sensitivities of the synthesizer, GPS receiver and USO. In the dataset shown in Extended Data Fig. 8, the average measured total temperature sensitivity was about 1.3×10^{-15} °C^{-1}. Coupled with the measured temperature variations, this sensitivity is unable to explain the peaks in the Allan deviation curve at either ~3×10^{5} s or ~1×10^{6} s or the general flattening above 1×10^{5} s. However, a more detailed analysis accounting for variations in the total temperature sensitivity, overall drift and other noise sources such as the measurement system and possibly the reference clock can explain these features. The 1-day sinusoidal temperature variation coupled with this sensitivity would result in an Allan deviation peak of $0.36\times0.5\,°C\times1.3\times10^{-15}\,°C^{-1}\approx2\times10^{-16}$ occurring at $0.37\times1\,day\approx3\times10^{4}$ s (ref. [30]). Similarly, the orbital variation would cause a peak of ~1×10^{-16} occurring at 2,200 s. Both are below the noise floor of the measurement. The small orbital peak in the measured Allan deviation in Extended Data Fig. 3 and in Fig. 4 is consistent with a peak in the simulated results shown in those figures. The simulation is based on measured sensitivities and measured orbital disturbance sizes. The resultant peak is dominated by USO temperature sensitivity with some contribution from temperature sensitivity to the differential synthesizer phase, which only manifests itself as a frequency shift when the temperature has a non-zero time derivative[30]. The USO is discussed in more detail below. The simulated Allan deviation in Extended Data Fig. 3 includes all known orbital clock disturbances (ions, synthesizers and USO, but not GPS) and shows that these disturbances are expected to be near or below the estimated noise floor.

Background pressure evolution

Frequency shifts due to background gas collisions generally do not limit clock operation if the vacuum chamber is properly prepared[40]. In the getter-pumped DSAC clock, the evolution of the CH_4 and H_2 partial pressures due to outgassing is measured on the ground to be well below 1×10^{-8} Pa per day. Noble gases are inactive and not pumped by the getter, but their frequency shift coefficients are several orders of magnitude below those of H_2 and CH_4 (refs. [41,42]) and insignificant on the scale considered here. H_2 is efficiently pumped by the in situ getter with a very high pumping speed, but CH_4 is only weakly interacting and pumped very slowly by 'cracking' into C and H_2 (both readily pumped) by a hot filament[43]. Owing to the high H_2 pumping speed, its partial pressure is likely to be very stable in the long term (>1 day). However, given the weak pumping speed of CH_4, it is possible that this could have a long-term evolution leading to a clock frequency drift. Here we place a limit on this variation. With a measured gas shift coefficient of -2.6×10^{-7} Pa^{-1} for CH_4 (refs. [41,42]), the corresponding frequency shift should be less than 3.5×10^{-15} per day. Extended Data Fig. 9 shows data taken when the trapped-ion number was very stable (>3 weeks after a power cycle, the clock frequency variations due to the number-dependent second-order Doppler shift are $<3\times10^{-16}$ per day). The next dominant effect is due to temperature variations, which can be reliably distinguished from a linear drift because the temperature has a turnover (it is not monotonic). The data are corrected for this measured temperature effect and then fitted to a straight line. The fitted slope is $2.7(5.3)\times10^{-21}$ s^{-1}, giving an upper bound on clock frequency variations due to trace gas evolution of 4.6×10^{-16} per day, which improves on the upper bound on CH_4 pressure variation to $<1.7\times10^{-9}$ Pa per day[44] (note that variations in trace-gas partial pressure due to temperature-driven outgassing rates would already have been absorbed into the overall temperature effect.) This is also consistent with the low overall clock drift observed for the longest operational run (see Fig. 3).

USO sensitivities

While the USO has its own temperature sensitivity, changes in the USO frequency due to temperature are, by design, highly suppressed by the clock control loop. Linear USO drift could result in an offset on the clock output frequency, but has no effect on the clock Allan deviation. However, nonlinear changes, such as a jump in the linear rate or a sinusoidal variation with temperature, will be present in both the output frequency and the Allan deviation. As these effects can limit clock performance, a USO drift compensation algorithm[8] is built into the clock control loop that reduces the impact of sudden changes in linear USO drift (rare) by a factor of 4 to 5 when calculated for current operational parameters. Of biggest concern to DSAC are orbital variations in USO temperature, and the full control algorithm with drift compensation is calculated to reduce the impact of these by 0.017 for current operational parameters, enough to prevent the prominent 2.8×10^{-12} peak-to-peak USO orbital disturbance from affecting clock performance beyond the small residual (USO-dominated) peak seen in the simulated curve of Extended Data Fig. 3.

Radiation effects and the South Atlantic Anomaly

When the clock was first turned on in space, an important observation was how it responded to the radiation doses received when passing through the South Atlantic Anomaly (SAA)[44]. This radiation is primarily high-energy protons with energies up to 100 MeV (ref. [45]). This radiation affects PMT counts and USO drift rate, both at levels that the control algorithm successfully mitigates.

Radiation-induced excess PMT counts is a well-established phenomenon and expected[46]. What is not as well-known is the quantitative response of a particular PMT to a given radiation environment and how it might affect the clock output. The two sources of detected PMT counts are ultraviolet light photons and radiation flux. Ultraviolet photons originate from the ultraviolet light source (or ion fluorescence stimulated by that source). The light source has two modes: a high-intensity bright mode that is used to prepare and read out the internal atomic states, and a low-intensity dim mode used during microwave interrogation. For the purpose of characterizing the radiation effect, sensitivity to it can be maximized by collecting data for the 8.1-s period in each clock cycle during which the light source is dim, thereby minimizing ultraviolet photon counts. Extended Data Fig. 10 shows the detected signal as a function of time during passes through the SAA while the light source is in the dim mode. During the dim mode,

the normal ultraviolet signal is 49,000 counts in 8.1 s. The peaks in the figure are caused by radiation flux corresponding to SAA transits and have a maximum slope of 80 counts s^{-1}. Normal clock operation consists of alternately interrogating the ions on either side of the clock transition and then differencing the ultraviolet fluorescence obtained during state readout when the ultraviolet light source is in the bright state. Normally, if the microwave interrogation is on frequency, the difference will be zero, otherwise not. Therefore, the varying detected counts caused by the radiation flux can appear to the clock algorithm as a drift. To quantitatively determine the impact of this radiation-induced slope on the clock when the ultraviolet source is in bright mode, we must multiply the maximum slope by the ratio of bright/dim detection times (3.5/8.1), which gives a maximum radiation-induced variation of 35 counts s^{-1}. The normal clock transition frequency sensitivity at half-height is 84,000 counts Hz^{-1}, so a radiation-induced excess of 35 counts s^{-1} could be interpreted as a 0.2-mHz or 5×10^{-15} fractional frequency shift per second. The clock control algorithm uses a windowing that compares the brightness on alternating sides of the resonance over the previous three cycles[30], in such a way that effects due to varying PMT counts, whether they are caused by radiation or the lamp itself, are highly suppressed. Higher-order impact is ruled out through modelling and through the lack of unexplained orbital peaks in the Allan deviation of the clock output.

The other observed impact of SAA transits has been on the USO drift rate. The accumulated USO response to radiation is slower, so explicit orbital variations are not resolved. Instead, a slow diurnal-like variation on the USO drift rate is observed. For the half-day that SAA passes occur, the USO has a higher drift rate than for the half-day that SAA passes do not occur. These two rates are very repeatable from one day to the next, resulting in a diurnal-like sinusoidal modulation on top of the average drift rate. This large 10^{-11} scale disturbance is filtered by the control algorithm to a level below the clock noise floor, largely because of its slow nature.

Data availability

Full data for Fig. 4 and Extended Data Fig. 3 are available from the corresponding author on reasonable request.

34. Larson, K. M. & Levine, J. Time transfer using the phase of the GPS carrier. In *Proc. 1998 IEEE International Frequency Control Symposium*, 292–297 (IEEE, 1998).
35. Bertiger, W. et al. Single receiver phase ambiguity resolution with GPS data. *J. Geod.* **84**, 327–337 (2010).
36. Petit, G. Sub-10^{-16} accuracy GNSS frequency transfer with IPPP. *GPS Solut.* **25**, 22 (2021).
37. Larson, K. M., Ashby, N., Hackman, C. & Bertiger, W. An assessment of relativistic effects for low earth orbiters: the GRACE satellites. *Metrologia* **44**, 484 (2007).
38. Prestage, J. D., Tjoelker, R. L., Dick, G. J. & Maleki, L. Doppler sideband spectra for ions in a linear trap. In *Proc. IEEE International Frequency Control Symposium*, 148–154 (IEEE, 1993).
39. Tjoelker, R. L., Prestage, J. D., Dick, G. J. & Maleki, L. Long term stability of Hg+ trapped ion frequency standards. In *Proc. 1993 IEEE International Frequency Control Symposium*, 132–138 (IEEE, 1993).
40. Burt, E. A. & Tjoelker, R. L. Prospects for ultra-stable timekeeping with sealed vacuum operation in multi-pole linear ion trap standards. In *Proc. 39th Annual Precise Time and Time Interval Systems and Applications Meeting*, 309–316 (Institute of Navigation, 2008).
41. Chung, S. K., Prestage, J. D. & Tjoelker, R. L. Buffer gas experiments in mercury (Hg^+) ion clock. In *Proc. IEEE International Frequency Control Symposium*, 130–133 (IEEE, 2004).
42. Yi, L., Taghavi-Larigani, S., Burt, E. A. & Tjoelker, R. L. Progress towards a dual-isotope trapped mercury ion atomic clock: further studies of background gas collision shifts. In *Proc. 2012 IEEE International Frequency Control Symposium*, 1–5 (IEEE, 2012).
43. Shen, G. L. The pumping of methane by an ionization assisted Zr/Al getter pump. *J. Vac. Sci. Technol. A* **5**, 2580 (1987).
44. Konradi, A., Badhwar, G. D. & Braby, L. A. Recent space shuttle observations of the South Atlantic Anomaly and the radiation belt models. *Adv. Space Res.* **14**, 911–921 (1994).
45. Ginet, G. P., Madden, D., Dichter, B. K. & Brautigam, D. H. Energetic Proton Maps for the South Atlantic Anomaly. In *Proc. 2007 IEEE Radiation Effects Data Workshop*, 1–8 (IEEE, 2007).
46. Jerde, R. L., Peterson, L. E. & Stein, W. Effects of high energy radiations on noise pulses from photomultiplier tubes. *Rev. Sci. Instrum.* **38**, 1387 (1967).

Acknowledgements This work is jointly funded by NASA's Space Technology Mission Directorate (STMD) office and the office of Space Communications and Navigation (SCaN). The research was carried out at the Jet Propulsion Laboratory, California Institute of Technology, under a contract with the National Aeronautics and Space Administration (80NM0018D0004). Copyright 2020, California Institute of Technology. Government sponsorship acknowledged.

Author contributions E.A.B., J.D.P. and R.L.T. contributed equally. E.A.B. led DSAC clock preparation and optimization, determined operation modes and parameters, characterized the clock and payload before launch and in space, and led manuscript preparation activity. J.D.P. is the DSAC clock co-investigator, led the vacuum tube, ion trap, optics and magnetic design, and consulted on all other aspects of clock preparation, characterization and data analysis. R.L.T. is the DSAC clock co-investigator, consulted on all aspects of clock and payload design, preparation, characterization and data analysis, and led efforts to resolve several technical challenges with the instrument. D.G.E. led the development of telemetry processing and analysis tools, characterized local oscillator and system performance, and performed USO and control loop modelling. D.K. contributed GPS data processing, modelling and analysis. D.W.M. led the GPS data processing, modelling and analysis, including relativistic calculations and orbital parameter analysis, and wrote telemetry processing and display software. D.E.R. led controller algorithm implementation and data acquisition, and coordinated clock commanding through the spacecraft provider. J.M.S. was the DSAC deputy principal investigator and led technical and programmatic planning and performed the new one-way navigation experiments enabled by DSAC. T.A.E. is the DSAC principal investigator, led technical and programmatic planning and performed the new one-way navigation experiments enabled by DSAC, and with D.W.M. devised new methods to perform GPS receiver thermal calibrations. R.T.W led USO characterizations, instrument integration into the payload and payload integration into the spacecraft. All authors read, edited and approved the final manuscript.

Competing interests The authors declare no competing interests.

Additional information
Correspondence and requests for materials should be addressed to E.A.B.
Peer review information *Nature* thanks Pascale Defraigne, Ekkehard Peik and the other, anonymous, reviewer(s) for their contribution to the peer review of this work.
Reprints and permissions information is available at http://www.nature.com/reprints.

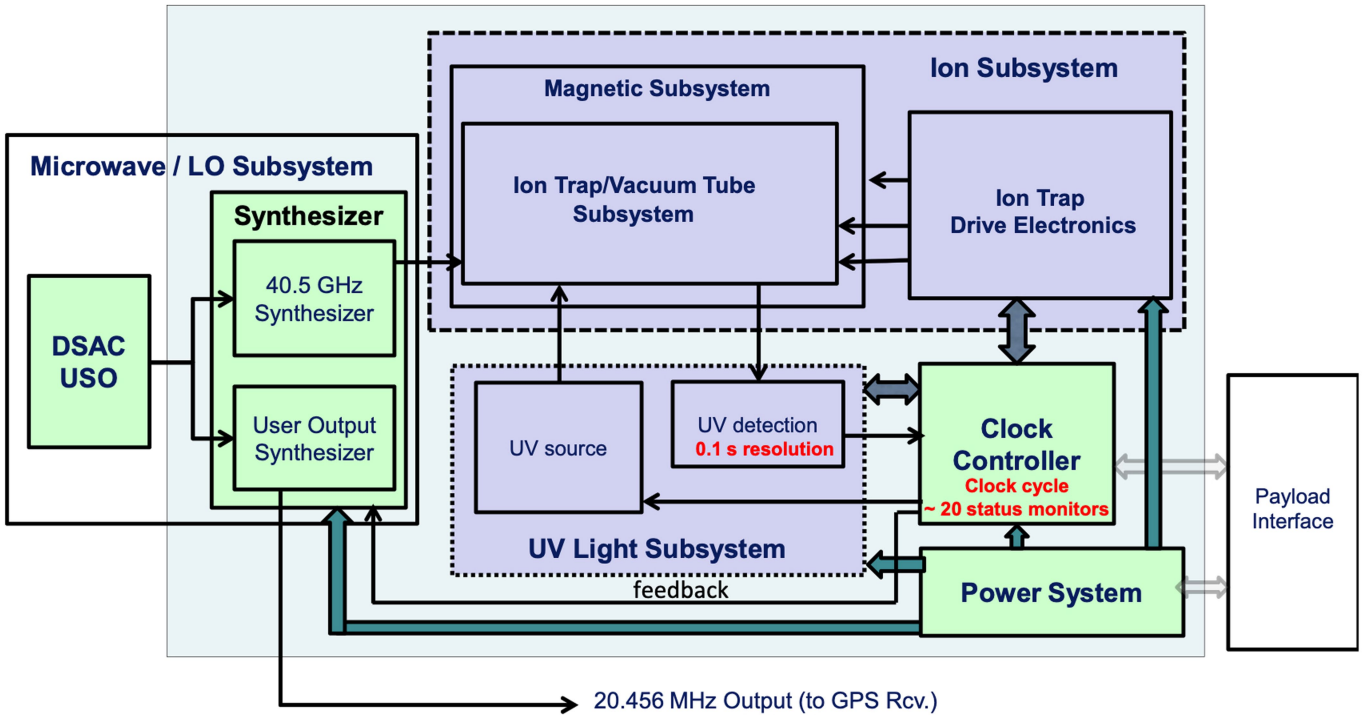

Extended Data Fig. 1 | System-level block diagram of the DSAC payload. The GPS receiver (Rcv.) is not shown.

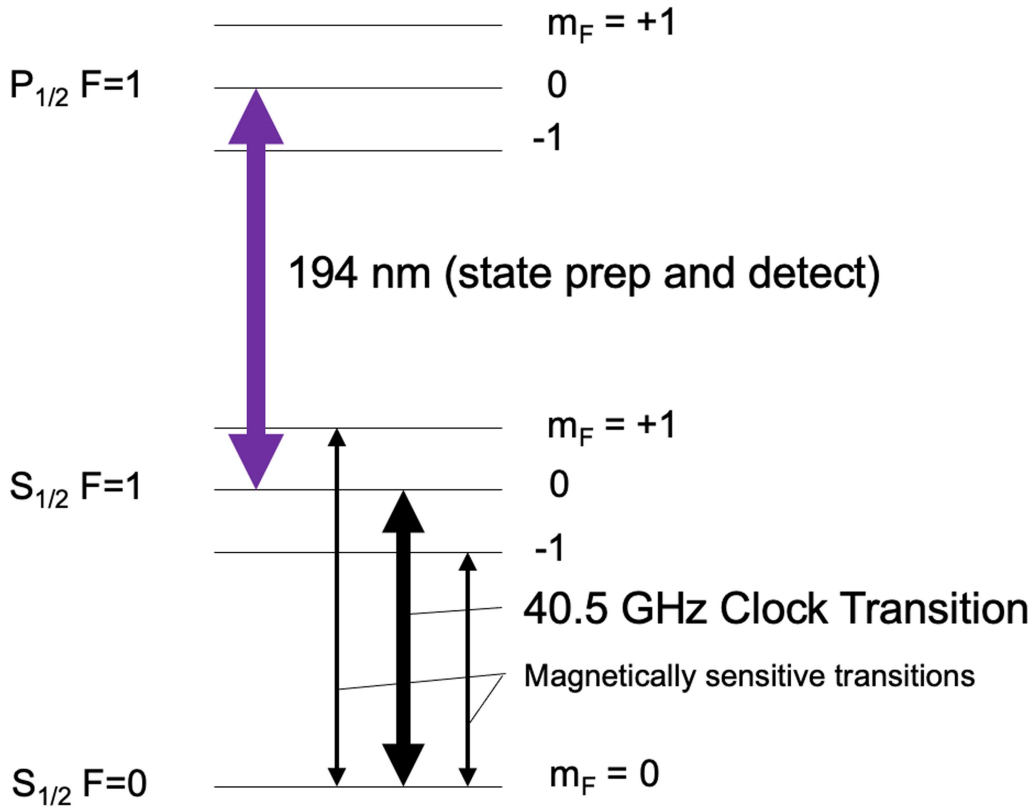

Extended Data Fig. 2 | Level diagram for ^{199}Hg(II). The $S_{1/2}$, $F=1$ to $P_{1/2}$, $F=1$ optical electric dipole transition used for state preparation and readout is shown in purple (note that the source of this light is broad enough to not resolve Zeeman sublevels, so the line is meant to indicate any transition between the $S_{1/2}$ $F=1$ and $P_{1/2}$ $F=1$ manifolds that is consistent with selection rules). Also shown are the $S_{1/2}$, $F=0$, $m_F=0$ to $S_{1/2}$, $F=1$, $m_F=0$ magnetic-field-insensitive 40.5-GHz hyperfine clock transition (thick black arrow), and the $\Delta m_F = \pm 1$ field-sensitive Zeeman lines at ±140 kHz (thin black arrows).

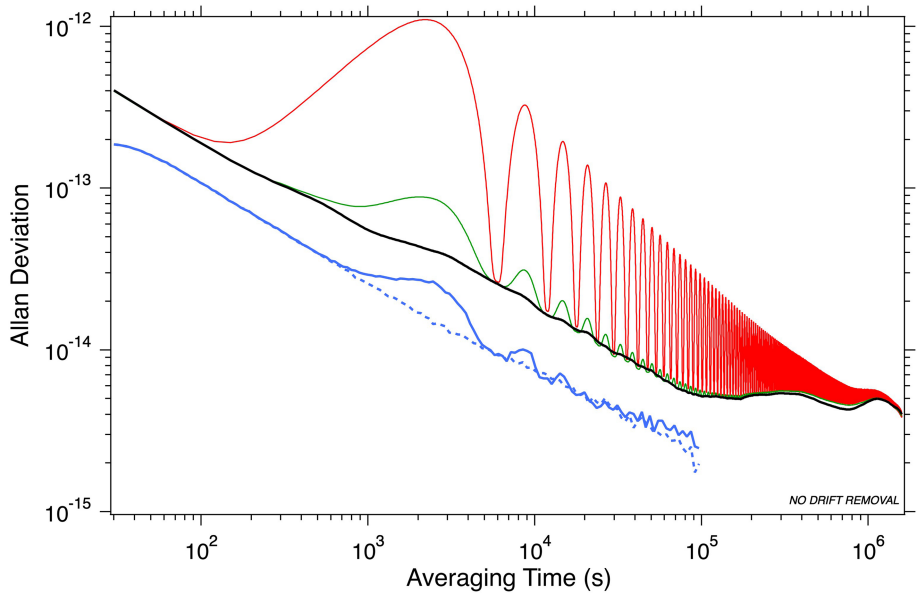

Extended Data Fig. 3 | Measured Allan deviation. Allan deviation without any corrections (red), with relativity corrections but no temperature corrections (green), and with both relativity and temperature corrections (black). Simulated expected clock performance with clock parameters during the run with environmental perturbations (solid blue) and without (dashed blue) is shown for comparison. All traces except the blue are overlapping Allan deviation. For reference, the orbital period of about $T = 6{,}000$ s will result in expected peaks in the Allan deviation at $0.37T \approx 2{,}200$ s (ref. [30]).

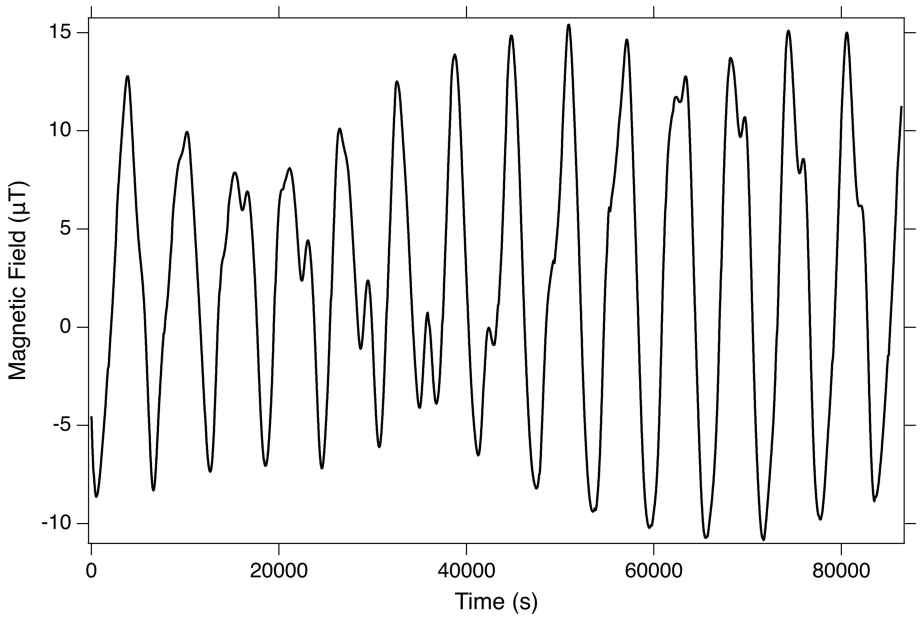

Extended Data Fig. 4 | Variations in the Earth's magnetic field observed on the DSAC spacecraft as a function of time. The orbital period is approximately 6,000 s at an altitude of 720 km. The component of the fieldin the weakest shielding direction is plotted. Shielding in the other two directions is over an order of magnitude higher so that the impact of variations on the clock is dominated by the component shown.

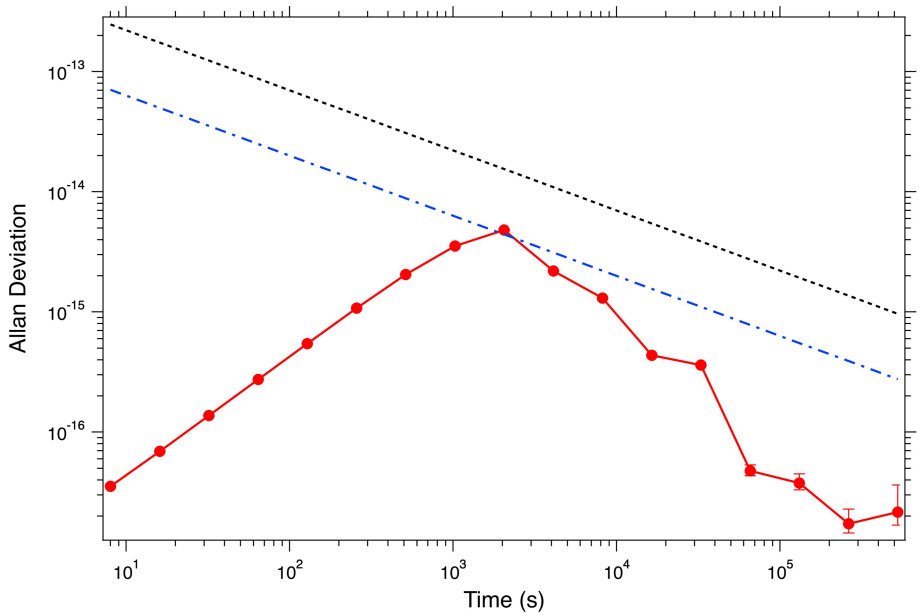

Extended Data Fig. 5 | Impact of magnetic field variations on the clock. The Allan deviation of the frequency shift associated with measured magnetic field variations on board the DSAC spacecraft is shown (red) assuming a worst-case sensitivity of $7 \times 10^{-16}\ \mu T^{-1}$. Reference lines are also shown for expected multipole trap (dashed blue) and load trap (dashed black) operation noise floors (without LO noise aliasing effects for the multipole trap line). Error bars represent 68% confidence intervals.

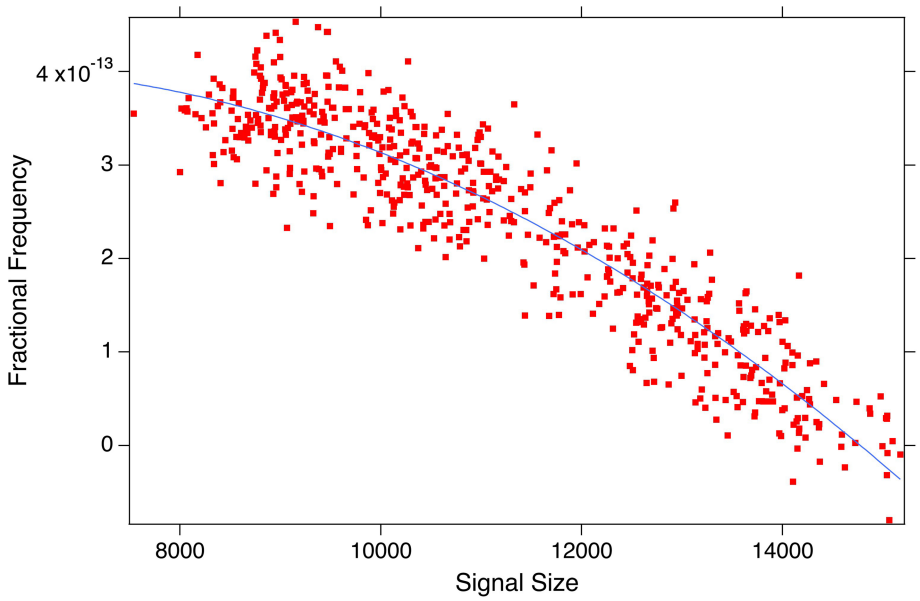

Extended Data Fig. 6 | Fractional frequency versus signal size in the load trap. Signal size is the number of PMT counts measured at the line centre minus the counts at a detuning of one linewidth corresponding to the first minimum in a Rabi line trace. The slope gives an estimate of the number-dependent second-order Doppler shift while operating in the load trap. As a point of reference, the corresponding shift in the multipole trap would be 10–20 times smaller.

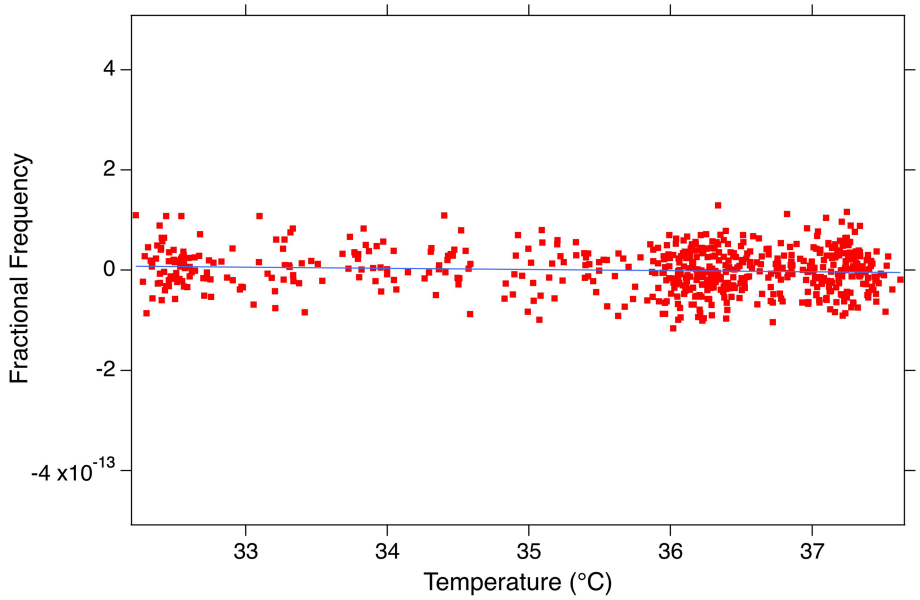

Extended Data Fig. 7 | Residuals from a fit to frequency versus signal size. Residuals are now plotted against temperature in the load trap. A linear fit gives a total temperature sensitivity of $-2.3(1.1) \times 10^{-15}\,°C^{-1}$.

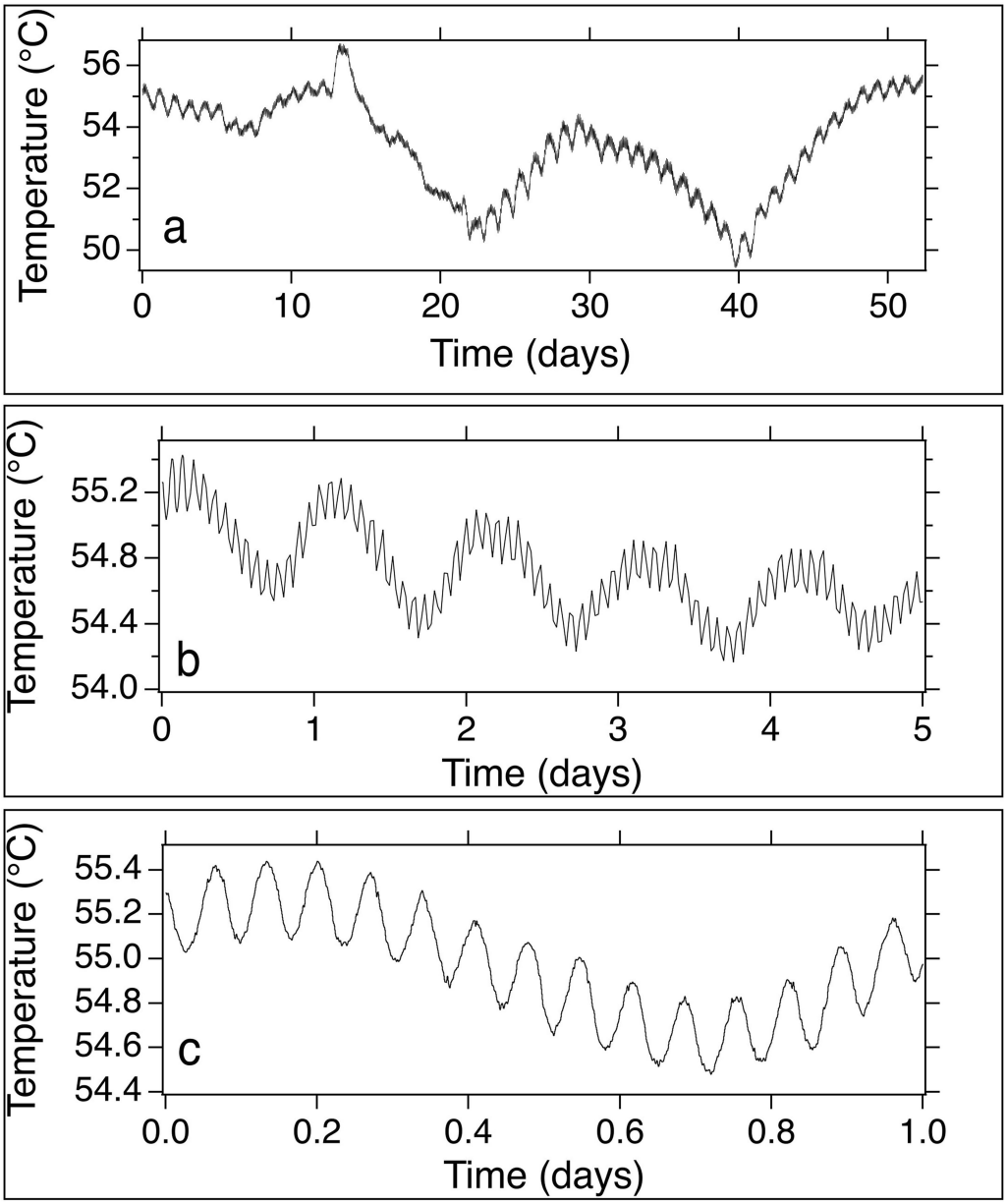

Extended Data Fig. 8 | Temperature data. Temperature data shown for the 52-day dataset described in the main text. **a**, Long-term temperature variation in the load trap over 52 days correlated with changes in Sun beta angle. **b**, A 5-day subset showing 24-h temperature variations. **c**, A 1-day subset showing orbital temperature variation.

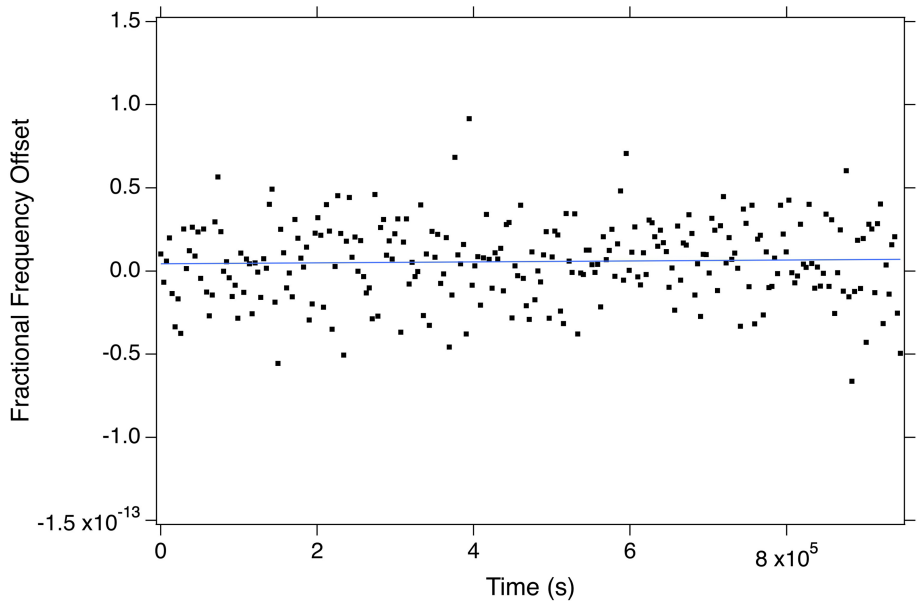

Extended Data Fig. 9 | Trace-gas evolution. Frequency data with the temperature effect removed (black dots) and fitted to a straight line (blue line), so as to place a limit of 4.6×10^{-16} per day on frequency shifts due to trace-gas evolution in the clock vacuum chamber.

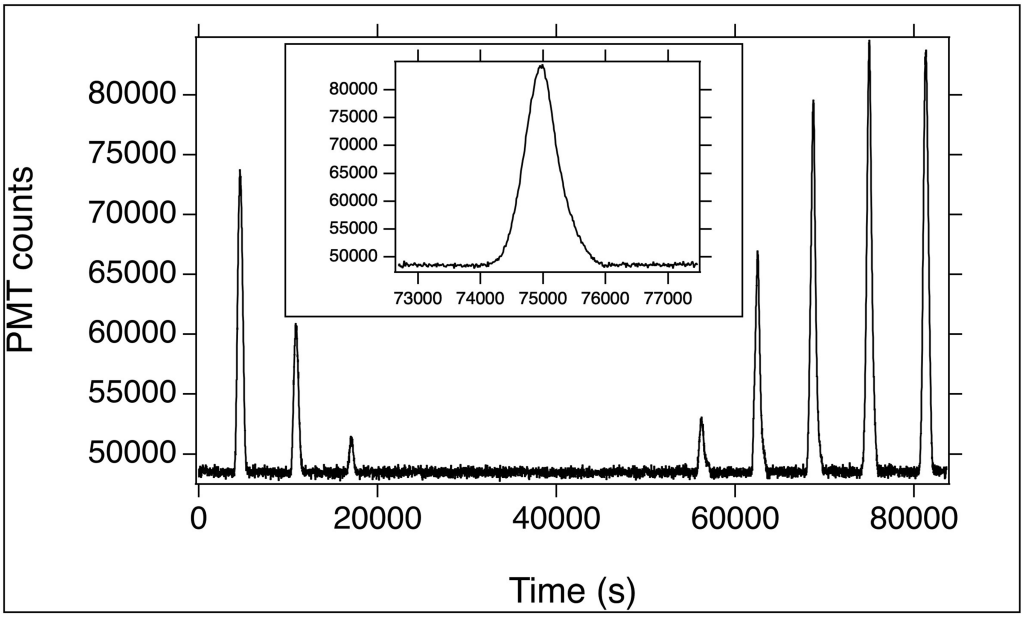

Extended Data Fig. 10 | Passage through the SAA. Total PMT counts in 8.1-s portions of each clock cycle as a function of time, showing excess counts due to passage through the SAA. Each passage is approximately 20 min, as shown for the expanded view (inset). The varying peak amplitude is due to spacecraft orbital precession, which varies the trajectory of the spacecraft in and out of the SAA on a daily timescale.